

Advanced phase-contrast techniques for wavefront sensing and adaptive optics

Mikhail A. Vorontsov^a, Eric W. Justh^b, Leonid A. Beresnev^a

^aIntelligent Optics Laboratory, U.S. Army Research Lab, Adelphi, MD 20783

^bInstitute for Systems Research, University of Maryland, College Park, MD 20742

ABSTRACT

High-resolution phase-contrast wavefront sensors based on optically addressed phase spatial light modulators and micro-mirror/LC arrays are introduced. Wavefront sensor efficiency is analyzed for atmospheric turbulence-induced phase distortions described by the Kolmogorov and Andrews models. A nonlinear Zernike filter wavefront sensor based on an optically addressed liquid crystal phase spatial light modulator is experimentally demonstrated. The results demonstrate high-resolution visualization of dynamically changing phase distortions within the sensor time response of about 10 msec.

Keywords: Zernike filter, adaptive optics, turbulence compensation, phase-contrast, wavefront sensing, phase measurement

1. INTRODUCTION

Wavefront phase sensing and spatial shaping (control) are important mutually related tasks. For most adaptive optics applications, the spatial resolution for wavefront sensing and wavefront correction are expected to match. This balance in resolution is easy to achieve in the case of low-resolution wavefront control systems. However, the situation is rapidly changing with the upcoming new generation of wavefront compensation hardware: high-resolution liquid crystal (LC) spatial phase modulators and micro-electromechanical systems (MEMS) containing large arrays of LC cells or micro-mirrors.¹⁻⁴ These new devices can potentially provide wavefront shaping with spatial resolution on the order of 10^4 – 10^6 elements. Such resolution is difficult to match with the traditional wavefront sensors used in adaptive optics: lateral shearing interferometer,^{5,6} Shack-Hartmann,⁷ curvature sensors,^{8,9} etc. In these sensors the wavefront phase is reconstructed from measurements of its first or second derivatives, which requires extensive calculations. When wavefront sensor resolution is increased by a factor of 10^2 – 10^3 , implementing this approach will lead to an unacceptable increase of phase reconstruction time, hardware complexity, and cost. Time-consuming calculations are also the main obstacle for wavefront sensors based on focal plane techniques: phase retrieval from a set of the pupil and focal plane intensity distributions,¹⁰⁻¹² phase diversity,^{13,14} and Schlieren techniques.¹⁵⁻¹⁷ For these methods the dependence of wavefront sensor output intensity (sensor output image) on phase is nonlinear, and phase reconstruction requires the solution of rather complicated inverse problems.

The problem of phase retrieval from high-resolution sensor data can to some degree be overcome by using a new adaptive optics control paradigm that utilizes the wavefront sensor output image directly without the preliminary phase reconstruction stage. This approach leads to high-resolution two-dimensional opto-electronic feedback adaptive system architectures.¹⁸⁻²⁰ In these systems a high-resolution wavefront corrector is interfaced with a wavefront sensor output camera, either directly or through opto-electronic hardware performing basic image processing operations, with the wavefront sensor output used “on-the-fly” and in parallel. The selection of the “right” wavefront sensor for such systems is a key problem.

High-resolution adaptive wavefront control and wavefront sensing are complimentary problems. When compensating phase distortions with an adaptive system, the phase reconstruction problem is automatically solved, as compensation results in the formation of a controlling phase matched to an unknown phase aberration (in the condition of perfect correction). From this viewpoint, high-resolution adaptive systems can be considered and used as parallel opto-electronic computational means for high-resolution wavefront phase reconstruction and analysis.

In Section 2, we describe new phase contrast sensor designs that can be used for high-resolution adaptive optics: differential, nonlinear, and opto-electronic Zernike filters. The differential Zernike filter (DZF) can provide phase visualization with increased contrast and accuracy. Standard phase visualization techniques are not effective for the analysis of dynamical phase aberrations containing wavefront tilts, e.g., aberrations induced by atmospheric turbulence. The

nonlinear and opto-electronic Zernike filters we consider, which are based on optically addressed phase spatial light modulators or on integrated micro-scale devices, are unresponsive to wavefront tilts and can be used for sensing dynamically changing wavefront distortions typical of atmospheric turbulence conditions. Numerical results of wavefront sensor performance analysis for the Kolmogorov and Andrews phase fluctuation spectra are discussed in Section 3. In Section 4 we present experimental results of wavefront phase distortion visualization using a nonlinear Zernike filter with a specially designed, optically addressed, nematic LC phase spatial light modulator.

2. HIGH-RESOLUTION PHASE VISUALIZATION WITH ZERNIKE FILTER AND SMARTT INTERFEROMETER

2.1. Mathematical models

The schematic for a conventional wavefront sensor based on the Zernike phase contrast technique (Zernike filter) is shown in Fig. 1a. It consists of two lenses with a phase-changing plate (Zernike phase plate) placed in the lenses' common focal plane. The phase plate has a small circular region (a dot) in the middle that introduces a phase shift θ near $\pi/2$ radians into the focused wave.^{15,16} The radius of the dot, a_F , is typically chosen to equal the diffraction-limited radius a_F^{dif} of a focused, undistorted input wave.

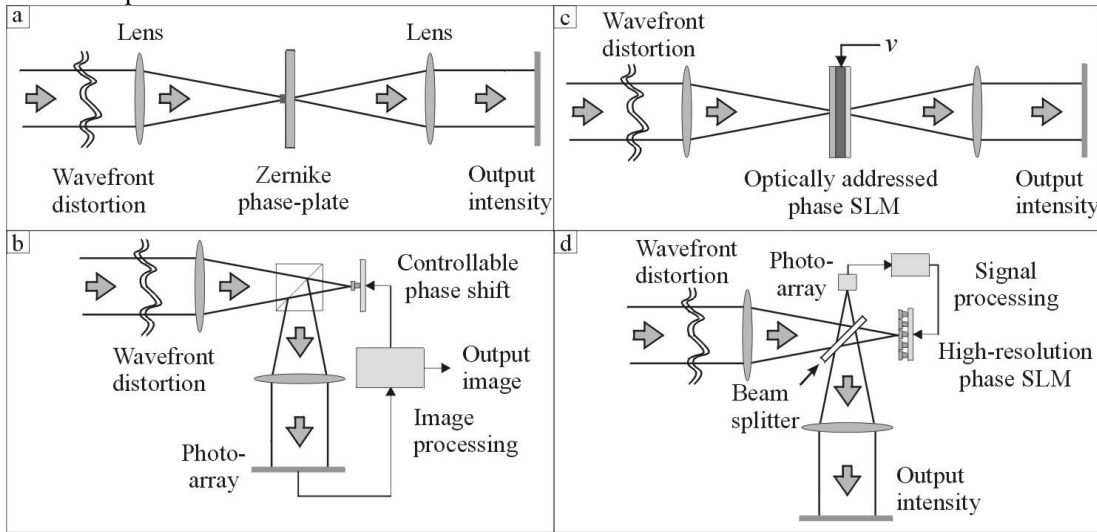


Fig. 1. Basic wavefront sensor schematics: (a) conventional; (b) differential; (c) nonlinear; and (d) opto-electronic Zernike filters.

In the case of the Smartt point-diffraction interferometer (PDI), the dot in the middle of the focal plane is absorbing. The absorption of light results in attenuation by a factor $\gamma < 1$ of the input wave low-frequency spectral components.²¹⁻²⁴ Both wavefront sensors can be described using a complex transfer function $T(\mathbf{q})$ for the focal-plane filter:

$$T(\mathbf{q}) = \gamma e^{i\theta} \text{ for } |\mathbf{q}| \leq q_0, \text{ and } T(\mathbf{q}) = 1 \text{ otherwise.} \quad (1)$$

The wave vector \mathbf{q} is associated with the focal plane radial vector \mathbf{r}_F through $\mathbf{q} = \mathbf{r}_F / (\lambda F)$, where F is the lens focal length, λ is wavelength, and $q_0 = a_F / (\lambda F)$ is the cutoff frequency corresponding to the dot size a_F . For the sake of convenience, consider the following variable normalization: the radial vectors \mathbf{r} in the sensor input/output plane and \mathbf{r}_F in the focal plane are normalized by lens aperture radius a , the wave vector \mathbf{q} by a^{-1} , and the lens focal length by the diffraction parameter ka^2 (where $k = 2\pi/\lambda$ is the wave number). Correspondingly, in the normalized variables $\mathbf{q} = \mathbf{r}_F / (2\pi F)$ and $q_0 = a_F / (2\pi F)$ (where the dot size a_F is also normalized by a).

From (1), when $\gamma=1$ and $\theta=\pi/2$, we have a Zernike filter model, and $\gamma=0$ corresponds to the PDI wavefront sensor. Consider a simplified model corresponding to a focal plane filter affecting only the zero-spectral component. In this case we have $T(0) = \gamma e^{i\theta}$ and $T(\mathbf{q})=1$ for $\mathbf{q} \neq 0$. Assume an input wave $A_{in}(\mathbf{r}) = A_0(\mathbf{r}) \exp[i\phi(\mathbf{r})]$ enters a wavefront sensor, where

$I_0(\mathbf{r}) = A_0^2(\mathbf{r})$ and $\varphi(\mathbf{r})$ are the input wave intensity and phase spatial distributions. The sensor's front lens performs a Fourier transform of the input wave. Within the accuracy of a phase factor, $A(\mathbf{q}) = (2\pi F)^{-1} F[A_{in}(\mathbf{r})]$, where $F[\]$ is the Fourier transform operator and $A(\mathbf{q})$ is the spatial spectral amplitude of the input field (i.e., the field complex amplitude in the focal plane).¹⁶ In normalized variables, the field intensity in the focal plane can be expressed as a function of spatial frequency: $I_F(\mathbf{q}) = (2\pi F)^{-2} |A(\mathbf{q})|^2$. The influence of the focal plane filter can be accounted for by multiplying $A(\mathbf{q})$ by the transfer function $T(\mathbf{q})$:

$$A_{out}(\mathbf{q}) = A(\mathbf{q})[1 - \delta(\mathbf{q})] + \gamma e^{i\theta} A(\mathbf{q})\delta(\mathbf{q}), \quad (2)$$

where $A_{out}(\mathbf{q})$ is the focal plane wave complex amplitude after passing through the spatial filter, and $\delta(\mathbf{q})$ is a delta-function. The wavefront sensor output field can be obtained by taking the Fourier transform of (2):

$$A_{out}(\mathbf{r}) = A_{in}(\mathbf{r}) - [1 - \gamma e^{i\theta}] \bar{A}, \quad (3)$$

where $\bar{A} = \int A_{in}(\mathbf{r}) d^2\mathbf{r}$ is the spatially averaged input field complex amplitude. For the sake of simplicity, we neglected the 180° rotation of the field performed by the wavefront sensor lens system.

Represent $\varphi(\mathbf{r})$ as a sum of the mean phase $\bar{\varphi}$ and spatially modulated deviation $\tilde{\varphi}(\mathbf{r})$: $\varphi(\mathbf{r}) = \bar{\varphi} + \tilde{\varphi}(\mathbf{r})$. In this case $\bar{A} = \exp(i\bar{\varphi})\bar{A}_0$, where $\bar{A}_0 = \int A_0(\mathbf{r}) \exp[i\tilde{\varphi}(\mathbf{r})] d^2\mathbf{r}$. The value of $|\bar{A}_0|^2$ is proportional to the field intensity at the center of the lens focal plane $I_F(\mathbf{q}=0) = (2\pi F)^{-2} |\bar{A}_0|^2$ (intensity of the zero spectral component). The normalized value of $I_F(0)$ is known as the Strehl ratio $St = I_F(0)/I_F^0$, where I_F^0 is the intensity of the zero spectral component in the absence of phase aberrations. With the introduced notation, equation (3) reads:

$$A_{out}(\mathbf{r}) = A_{in}(\mathbf{r}) - [1 - \gamma e^{i\theta}] \bar{A}_0 \exp(i\bar{\varphi}). \quad (4)$$

As we see from (4), the output field is a superposition of the input and spatially uniform reference wave components. Represent the complex value \bar{A}_0 in the following form: $\bar{A}_0 \equiv |\bar{A}_0| \exp(i\Delta) = (2\pi F) I_F^{1/2}(0) \exp(i\Delta)$, where $I_F(0)$ and Δ are the intensity and phase of the zero-order spectral component. The intensity distribution in the wavefront sensor output plane is given by

$$I_{out}(\mathbf{r}) = I_0(\mathbf{r}) + (2\pi F)^2 I_F(0) (1 + \gamma^2 - 2\gamma \cos\theta) - 4\pi F I_0^{1/2}(\mathbf{r}) I_F^{1/2}(0) \{ \cos[\tilde{\varphi}(\mathbf{r}) - \Delta] - \gamma \cos[\tilde{\varphi}(\mathbf{r}) - \Delta - \theta] \}. \quad (5)$$

The output intensity (5) is similar to the typical interference pattern obtained in a conventional interferometer with reference wave – the intensity is a periodic function of the wavefront phase modulation. For the case of the point diffraction interferometer, $\gamma=0$ and:

$$I_{out}(\mathbf{r}) = I_0(\mathbf{r}) + (2\pi F)^2 I_F(0) - 4\pi F I_0^{1/2}(\mathbf{r}) I_F^{1/2}(0) \cos[\tilde{\varphi}(\mathbf{r}) - \Delta]. \quad (6)$$

For an ideal Zernike filter ($\gamma=1$ and $\theta = \pi/2$), from (5) we obtain:

$$I_{out}(\mathbf{r}) \equiv I_{zer}^{(+)}(\mathbf{r}) = I_0(\mathbf{r}) + 2(2\pi F)^2 I_F(0) - 4\pi F I_0^{1/2}(\mathbf{r}) I_F^{1/2}(0) \{ \cos[\tilde{\varphi}(\mathbf{r}) - \Delta] - \sin[\tilde{\varphi}(\mathbf{r}) - \Delta] \}. \quad (7)$$

2.2. Wavefront sensor performance metrics

An important characteristic of the wavefront sensor is the output pattern visibility defined as $\Gamma = (\max I_{out} - \min I_{out}) / (\max I_{out} + \min I_{out})$. For the point diffraction interferometer and Zernike filter we have:

$$\Gamma_{PDI}(\mathbf{r}) = 4\pi F I_0^{1/2}(\mathbf{r}) I_F^{1/2}(0) / [I_0(\mathbf{r}) + (2\pi F)^2 I_F(0)], \quad (8)$$

$$\Gamma_{ZF}(\mathbf{r}) = 4\sqrt{2}\pi F I_0^{1/2}(\mathbf{r}) I_F^{1/2}(0) / [I_0(\mathbf{r}) + 2(2\pi F)^2 I_F(0)]. \quad (9)$$

In contrast with conventional interferometers, the visibility functions (8) and (9) are dependent on the input wave phase modulation $\tilde{\varphi}(\mathbf{r})$ through the term $I_F(0)$. In adaptive optics the phase aberration amplitude is continuously changing. This dependence may lead to negative effects, such as a continuous variation in the wavefront sensor output pattern contrast. Besides visibility, the contrast of the wavefront sensor output can be characterized using the aperture-averaged variance σ_I of the output intensity modulation $\tilde{I}_{out}(\mathbf{r}) = I_{out}(\mathbf{r}) - \bar{I}_{out}$:

$$\sigma_I = [S^{-1} \int \tilde{I}_{out}^2(\mathbf{r}) d^2\mathbf{r}]^{1/2}, \quad (10)$$

where \bar{I}_{out} is the aperture-averaged output intensity (DC component), and $S = \pi a^2$ is the aperture area.

Another important wavefront sensor characteristic is the sensor's nonlinearity; that is, the nonlinearity of the phase-intensity transformation $I_{out}[\varphi]$ performed by the wavefront sensor. A desirable (ideal) wavefront sensor should provide both high output pattern contrast and a linear dependence between the output intensity and input phase: $I_{out}(\mathbf{r}) = \kappa \tilde{\varphi}(\mathbf{r}) + \bar{I}_{out}$, where κ is a coefficient. Wavefront sensor nonlinearity can be characterized by the correlation between the phase $\tilde{\varphi}(\mathbf{r})$ and the output intensity modulation $\tilde{I}_{out}(\mathbf{r})$. As a nonlinearity metric, define the following phase-intensity correlation coefficient $c_{\varphi,I}$:

$$c_{\varphi,I} = \frac{1}{S \sigma_{\varphi} \sigma_I} \int \tilde{\varphi}(\mathbf{r}) \tilde{I}_{out}(\mathbf{r}) d^2\mathbf{r}, \text{ where } \sigma_{\varphi} = [S^{-1} \int \tilde{\varphi}^2(\mathbf{r}) d^2\mathbf{r}]^{1/2}. \quad (11)$$

For the ideal wavefront sensor, $c_{\varphi,I} = 1$. Note that strong wavefront sensor nonlinearity (a low value of the correlation coefficient) does not mean that the wavefront sensor can not be used for high-resolution wavefront analysis and adaptive control. Examples of high-resolution adaptive systems based on highly nonlinear wavefront sensors are the adaptive interferometers^{20,25,26} and diffractive-feedback adaptive systems.^{18,19} Nevertheless, "weak nonlinearity" offers an easier way to use a wavefront sensor for both wavefront analysis and wavefront control, providing for more efficient system architectures. For wavefront reconstruction methods based on iterative techniques, "quasi-linear" wavefront sensor output can be used as an initial wavefront phase approximation resulting in fast iterative process convergence.¹² For adaptive optics "weak nonlinearity" allows implementation of simple feedback control architectures when sensor output intensity is directly used to drive a high-resolution phase modulator.

Both characteristics of wavefront sensor performance – the correlation coefficient $c_{\varphi,I}$ and the standard deviation of the sensor output σ_I normalized by \bar{I}_{out} – can be combined into a single wavefront sensor performance metric

$$Q_{\varphi} = c_{\varphi,I} \sigma_I / \bar{I}_{out} = \frac{1}{\sigma_{\varphi} \bar{I}_{out} S} \int \tilde{\varphi}(\mathbf{r}) \tilde{I}_{out}(\mathbf{r}) d^2\mathbf{r}. \quad (12)$$

2.3. Differential Zernike filter

The visibility of the ideal Zernike filter output pattern can be significantly increased by using a focal phase plate with controllable phase shift switching between two states: $\theta = \pi/2$ and $\theta = -\pi/2$ (or $\theta = 3\pi/2$). For a phase shift of $\theta = -\pi/2$ (or $\theta = 3\pi/2$), the output intensity distribution (5) reads:

$$I_{out}(\mathbf{r}) \equiv I_{zer}^{(-)}(\mathbf{r}) = I_0(\mathbf{r}) + 2(2\pi F)^2 I_F(0) - 4\pi F I_0^{1/2}(\mathbf{r}) I_F^{1/2}(0) \{ \cos[\tilde{\varphi}(\mathbf{r}) - \Delta] + \sin[\tilde{\varphi}(\mathbf{r}) - \Delta] \}. \quad (13)$$

The difference between the intensity distributions (7) and (13),

$$I_{dif}(\mathbf{r}) \equiv I_{zer}^{(+)}(\mathbf{r}) - I_{zer}^{(-)}(\mathbf{r}) = 8\pi F I_0^{1/2}(\mathbf{r}) I_F^{1/2}(0) \sin[\tilde{\varphi}(\mathbf{r}) - \Delta], \quad (14)$$

does not contain a DC term. The visibility of the output pattern (14) is higher than what can be obtained using a conventional Zernike filter, and is limited only by the noise level. The "price" paid for this visibility increase is that additional computations should be performed using two output images. The differential Zernike wavefront sensor can be built using a controllable phase-shifting plate containing a single LC or MEMS actuator interfaced with the output photo-array and image subtraction system, as shown in Fig. 1b. Output intensity registration and processing (subtraction) capabilities can be integrated in a specially designed VLSI imaging chip.^{27,28}

2.4. Nonlinear Zernike filter

Both the Zernike filter and point diffraction interferometer are not efficient in the presence of significant amplitude wavefront tilts, e.g., in the presence of atmospheric turbulence-induced phase distortions. Wavefront tilts cause displacement of the focused wave with respect to the filter's phase-shifting (absorbing) dot. When displacements are large enough, the focused beam can miss the dot.

To remove dependence of the phase visualization on wavefront tilts, the position of the phase shifting dot in the Zernike filter should adaptively follow the position of the focal field intensity maximum (focused beam center). This self-

adjustment of phase dot position can be achieved in the nonlinear Zernike filter proposed by Ivanov, et. al.¹² In the nonlinear Zernike filter the phase shifting plate is replaced by an optically addressed phase spatial light modulator (OA phase SLM), as shown in Fig. 1c. The phase SLM introduces a phase shift θ dependent on the focal plane intensity distribution $I_F(\mathbf{q})$, i.e., $\theta = \theta(I_F)$. In the simplest case the dependence $\theta = \theta(I_F)$ is linear: $\theta = \alpha I_F$, where α is a phase modulation coefficient. A linear dependence between phase shift and light intensity is widely known in nonlinear optics as Kerr-type nonlinearity.¹⁷ Correspondingly, the influence of the OA phase SLM on the transmitted (or reflected) wave is similar to the influence of a thin layer of Kerr-type nonlinear material (Kerr slice).¹⁷ For the nonlinear Zernike filter, the spectral amplitude of the field in the lens focal plane (after passing the OA phase SLM) reads:

$$A_{out}(\mathbf{q}) = A(\mathbf{q}) \exp[i\alpha I_F(\mathbf{q})], \text{ where } I_F(\mathbf{q}) = (2\pi F)^{-2} |A(\mathbf{q})|^2. \quad (15)$$

The optically addressed phase SLM in the nonlinear Zernike filter causes a phase shift of all spectral components. For small amplitude phase distortions, phase shifts of higher-order components are smaller than the phase shift of the zero component, which has a much higher intensity level. In this case the nonlinear Zernike filter behaves similar to the conventional Zernike wavefront sensor with a phase-shifting dot. In the nonlinear Zernike filter a “phase dot” is created at the current location of the focused beam center, and follows the focused beam displacement caused by wavefront tilts. The effective “dot size” in the nonlinear Zernike filter is dependent on the intensity distribution of low spectral components. The phase modulation coefficient α in (15) can be optimized to provide a maximum phase shift near $\pi/2$ for the central spectral component: $\theta_{max} = \alpha I_F(\mathbf{q}_c) = \alpha \max[I_F(\mathbf{q})] \cong \pi/2$. In the case of the liquid crystal light valve (LCLV) SLM described in Section 4, the coefficient α can be adjusted by controlling the voltage applied to the phase SLM.^{1,29} Like the conventional Zernike filter, the nonlinear Zernike filter suffers from the problem of a strong dependence of the output pattern contrast on phase modulation amplitude.

2.5. Opto-electronic Zernike filters

Both high sensitivity to wavefront tilts and the strong dependence of phase visualization contrast on aberration amplitude can be reduced by using the opto-electronic Zernike filter shown in Fig. 1d. The wavefront sensor consists of a high-resolution phase SLM, for example a LC-on-silicon chip phase SLM,⁴ and a photo-array optically matched to the phase modulator in the sense that both devices have the same size and pixel geometry. The beam splitter in Fig. 1d provides two identical focal planes. The photo-array interfaces with the phase SLM to provide programmable feedback. Depending on the complexity of the feedback computations, signal processing may be performed directly on the imager chip using very large system integration (VLSI) micro-electronic systems.^{27,28} In this case the VLSI imager system can be coupled directly to the phase SLM.

The VLSI imager chip interfaced to the phase SLM can track the location of the focused beam center and shift the phase of the central spectral component in the SLM plane by $\pi/2$. The opto-electronic Zernike filter operates similar to the conventional Zernike filter with the phase-shifting dot, except that it is not sensitive to wavefront tilts. The programmable feedback between the imager chip and phase SLM can be used to design an opto-electronic nonlinear Zernike filter ($\theta = \alpha I_F$), or provide an even more complex dependence of the phase shift on the focal intensity distribution $\theta = \theta(I_F)$. This processing may include, for example, intensity thresholding: $\theta = \pi/2$ for all spectral components \mathbf{q} for which $I_F(\mathbf{q}) \geq \varepsilon \max[I_F(\mathbf{q})]$ and $\theta = 0$ otherwise, where $0 < \varepsilon \leq 1$ is a coefficient. Using advanced optical MEMS, LC SLM, and VLSI technologies, the opto-electronic Zernike wavefront sensor can potentially be implemented as an integrated device. To increase the sensor’s output pattern contrast, the opto-electronic Zernike filter can be incorporated with the differential wavefront sensor scheme described above.

3. WAVEFRONT SENSOR PERFORMANCE ANALYSIS FOR ATMOSPHERIC TURBULENCE-INDUCED DISTORTIONS

3.1. Numerical model

We compared the performance of the wavefront sensors described here using the Kolmogorov³⁰ and Andrews³¹ models for atmospheric turbulence-induced phase fluctuation power spectra:

$$G_K(q) = 2\pi \cdot 0.033 (1.68/r_0)^{5/3} q^{-11/3}, \quad (16a)$$

$$G_A(q) = 2\pi \cdot 0.033 (1.68/r_0)^{5/3} (q^2 + q_A^2)^{-11/6} \exp(-q^2/q_A^2) [1 + 1.802(q/q_A) - 0.254(q/q_A)^{7/6}]. \quad (16b)$$

Here r_0 is the Fried parameter,³² $q_A = 2\pi / l_{out}$, and $q_a = 2\pi / l_{in}$, where l_{out} and l_{in} are the outer and inner scales of turbulence. In the Andrews model, the large and small scale phase distortion contributions are dependent on the outer and inner scale parameters. In comparison with the Andrews spectrum, in the Kolmogorov model low spatial frequencies are more dominant.

Simulations were performed for an input wave having a uniform intensity distribution $I_0(\mathbf{r}) = I_0$ and random phase $\varphi(\mathbf{r})$ determined inside a circular aperture of diameter D . For the phase aberrations $\varphi(\mathbf{r})$ we used an ensemble of 200 realizations of a statistically homogeneous and isotropic random function $\varphi(\mathbf{r})$ with zero mean and spatial power spectra (16). The numerical grid was 256×256 pixels with a wavefront sensor aperture corresponding to 0.85 of the grid size. In the Andrews model we used $l_{out} = 1.2D$ and l_{in} was equal to the grid element size. The input wavefront phase distortions were characterized by both the standard deviation of the phase fluctuations averaged over the aperture $\sigma_{in} = \langle \sigma_\varphi \rangle = \langle [S^{-1} \int \tilde{\varphi}^2(\mathbf{r}) d^2\mathbf{r}]^{1/2} \rangle$, and the averaged Strehl ratio $\langle St \rangle$ calculated with wavefront tilts removed, where $\langle \rangle$ denotes ensemble averaging over the phase distortion realizations.

3.2. Numerical analysis: phase aberration visualization

Consider first the results of the numerical analysis performed for a single realization of the phase aberration $\varphi(\mathbf{r})$ corresponding to the Andrews model (16b), for different values of the Fried parameter r_0 . Output intensity patterns for the opto-electronic Zernike filter are shown in Fig. 2. The opto-electronic Zernike filter provides a $\pi/2$ phase shift for the spectral component having the highest intensity level independent of the current location of this component. In this way, the effects of wavefront tilts are removed. For relatively small amplitude phase distortions ($\sigma_\varphi < 0.4$ rad. and $St > 0.85$), the sensor's intensity pattern is similar to the phase distribution $\varphi(\mathbf{r})$, which suggests that the dependence $I_{out}[\varphi]$ is "quasi-linear". In this regime the wavefront sensor provides good quality visualization of the phase distortion, as seen in Fig. 2a-c. When the phase distortion amplitude increases ($\sigma_\varphi > 1.5$ rad., $St < 0.1$), the match between output intensity and input phase vanishes, indicating a highly nonlinear phase-intensity transformation $I_{out}[\varphi]$ performed by the wavefront sensor (Fig. 2d). In this regime the contrast of the output pattern is also decreased.

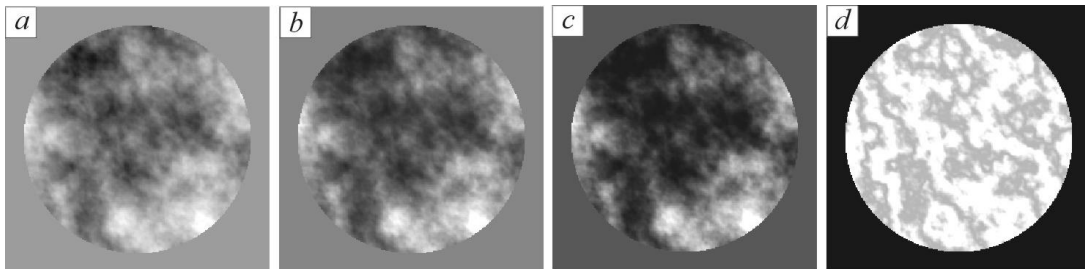


Fig. 2. Output intensity patterns for the opto-electronic Zernike filter corresponding to the input phase realization with Andrews spectrum (a) for different σ_φ values; (b) $\sigma_\varphi = 0.23$ rad., (c) $\sigma_\varphi = 0.41$; and (d) $\sigma_\varphi = 2.45$.

Output pattern contrast can be increased using the opto-electronic Zernike filter with the intensity thresholding described earlier. The sensor output pattern in Fig. 3b corresponds to intensity thresholding, where the phase was shifted by $\theta = \pi/2$ for all spectral components \mathbf{q} satisfying $I_F(\mathbf{q}) \geq 0.75 \max[I_F(\mathbf{q})]$. The increase in output pattern visibility does not result in linearization of the wavefront sensor output: for large phase distortion amplitudes the dependence $I_{out}[\varphi]$ remains highly nonlinear.

Samples of output intensity patterns for the nonlinear Zernike filter are presented in Fig. 4. Optimization of the phase modulation coefficient α in (15) allowed us to obtain good quality visualization of phase distortions in the range up to $\sigma_\varphi \cong 1.0$ rad. ($St \cong 0.3$). With further phase distortion amplitude increase, degradation of both the sensor output contrast and correlation between I_{out} and φ were observed (Fig. 4d).

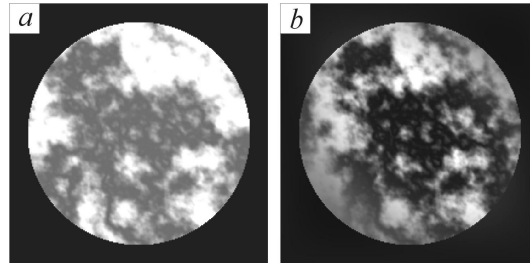


Fig. 3. Contrast enhancement in the opto-electronic Zernike filter with intensity thresholding. Output intensity patterns for the opto-electronic Zernike filter without (a) and with (b) intensity thresholding ($\epsilon = 0.75$) corresponding to the input phase realization with Andrews spectrum shown in Fig. 2(a). In both cases the standard deviation for the aperture-averaged phase deviation is $\sigma_\varphi = 1.48$ rad. ($St=0.1$).

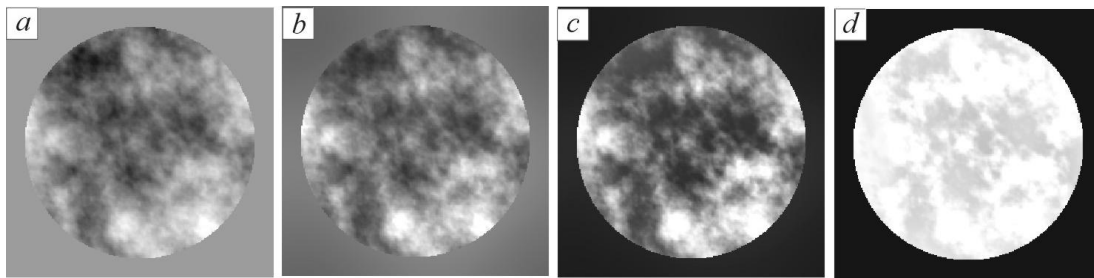


Fig. 4. Output intensity patterns for the nonlinear Zernike filter corresponding to the input phase realization with Andrews spectrum (a) for $\alpha = 0.5\pi / I_F^0$ and different σ_φ : (b) $\sigma_\varphi = 0.23$ rad., (c) $\sigma_\varphi = 0.72$ rad. and (d) $\sigma_\varphi = 1.48$ rad. The value I_F^0 is the zero spectral component intensity in the absence of phase aberrations.

In contrast with the Zernike filter, the dependence $I_{out}[\varphi]$ for the point diffraction interferometer is nonlinear even for phase distortions with small amplitudes. This means that the use of the point diffraction interferometer for phase analysis and adaptive wavefront control requires additional processing of the sensor output.

3.3. Numerical analysis: phase aberration visualization

Statistical analysis of wavefront sensor efficiency was performed for the following wavefront sensors: opto-electronic Zernike filter, point diffraction interferometer, nonlinear Zernike filter having different values of the phase modulation coefficient α , and opto-electronic Zernike filter with intensity thresholding. To analyze the impact of phase distortion amplitude on wavefront sensor performance, the Fried parameter r_0 in (16) was varied from $r_0 = 1.5D$ to $r_0 = 0.1D$. Correspondingly, for each value of r_0 , two hundred phase distortion realizations were generated. Wavefront sensor performance was evaluated using the standard deviation of the output intensity σ_I (10), the phase-intensity correlation coefficient $c_{\varphi,I}$ (11), and the wavefront sensor performance metric Q_φ (12). Values of σ_I , $c_{\varphi,I}$ and Q_φ calculated for each of 200 random phase screen realizations were averaged to obtain an approximation of the corresponding ensemble averaged parameters $\sigma_{out} = \langle \sigma_I / \bar{I}_{out} \rangle$, $C = \langle c_{\varphi,I} \rangle$, and $Q = \langle Q_\varphi \rangle$, presented in Figs. 5 and 6 as functions of the input phase standard deviation σ_{in} .

The standard deviation of wavefront sensor output intensity fluctuation, σ_{out} , shown in Fig. 5 (left), characterizes the contrast of the sensor output image. All curves in Fig. 5 (left) decay for both small and large amplitude phase distortions, with maximum contrast corresponding to the region $\sigma_{in} \cong 0.5 - 0.7$ rad. The highest phase visualization contrast was observed for the nonlinear Zernike filter, the lowest one for the point diffraction interferometer.

The phase-intensity correlation coefficients presented in Fig. 5 (right) characterize the similarity between the sensor's input phase and output intensity. The phase aberration range ($0 < \sigma_{in} \leq \sigma_{in}^0$) corresponding to a correlation coefficient value near unity ($C > C_0$) specifies the quasi-linear regime of wavefront sensor operation. For the opto-electronic Zernike filter and sensor with intensity thresholding, for $C_0 = 0.9$, the quasi-linear operational range corresponded to $\sigma_{in}^0 \cong 0.66$ rad. ($St \cong 0.64$). In the case of the nonlinear Zernike filter with $\alpha = 0.5\pi/I_F^0$, this range was extended up to $\sigma_{in}^0 \cong 1.0$ rad. ($St \cong 0.33$). The differential Zernike filter has the widest quasi-linear range, due to the cancellation of second-order nonlinear terms by the image subtraction $I_{zer}^{(+)}(\varphi) - I_{zer}^{(-)}(\varphi)$.

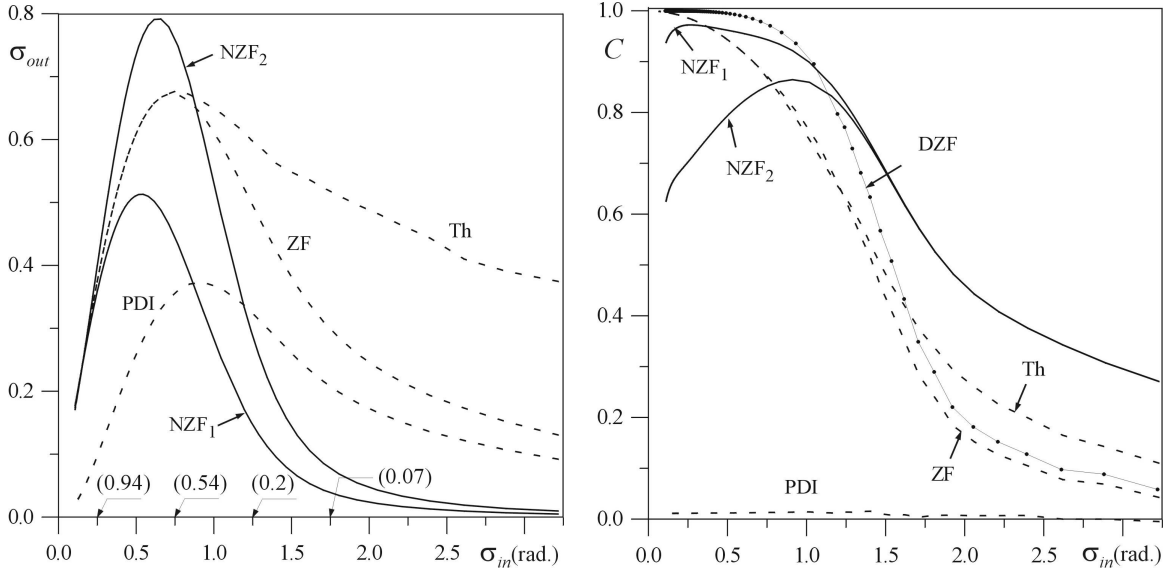


Fig. 5. (Left) Standard deviation of output intensity fluctuations σ_{out} for different wavefront sensor types vs. input phase standard deviation σ_{in} (Andrews spectrum). Dashed curves correspond to the following opto-electronic wavefront sensor configurations: point diffraction interferometer (PDI), Zernike filter (ZF), and opto-electronic Zernike filter with intensity thresholding (Th) for $\varepsilon = 0.5$. Solid curves correspond to nonlinear Zernike filter with $\alpha = 0.5\pi/I_F^0$ (NZF₁) and $\alpha = \pi/I_F^0$ (NZF₂). Numbers in brackets correspond to Strehl ratio values $\langle St \rangle$ for σ_{in} . (Right) Phase-intensity correlation coefficients C vs. input phase standard deviation σ_{in} (Andrews spectrum). Solid curve with dots corresponds to the differential Zernike filter (DZF).

Summarized results for the wavefront sensor quality metric Q are presented in Fig. 6 (left). The best performance metric value was achieved by using the nonlinear Zernike filter with $\alpha = \pi/I_F^0$. The opto-electronic Zernike filter with intensity thresholding had the widest operational range. The quality metric Q in the form (12) is not applicable for the differential Zernike filter because the aperture-averaged output \bar{I} in (12) equals zero – a result of the DC component subtraction. In the absence of noise, the phase-intensity correlation coefficient C can be considered as a performance quality metric for the differential Zernike filter.

The corresponding results for wavefront sensor performance metrics obtained for the Kolmogorov phase fluctuation spectrum are presented in Fig. 6 (right). They are similar to the Andrews model except the operational range for Kolmogorov turbulence is wider. Results of calculations for both the Kolmogorov and Andrews models show that the wavefront sensors can provide effective visualization of phase distortions over a wide range of phase distortion amplitudes. By using the differential scheme as well as the nonlinear Zernike filter with an adaptively changing phase modulation coefficient, sensor operational range can be further extended.

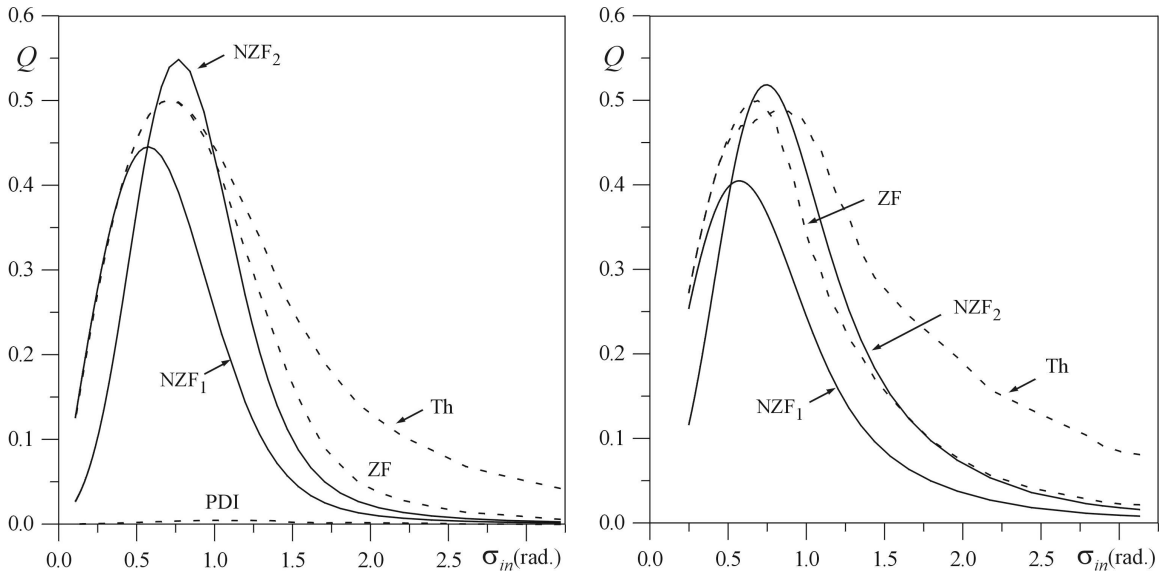


Fig. 6. (Left) Wavefront sensor performance metric Q vs. input phase standard deviation σ_{in} (Andrews spectrum). Notations are the same as in Fig. 5. (Right) Wavefront sensor performance metric Q vs. input phase standard deviation σ_{in} (Kolmogorov spectrum).

4. WAVEFRONT SENSING WITH NONLINEAR ZERNIKE FILTER: EXPERIMENTAL RESULTS

4.1. Liquid crystal light valve phase modulator for nonlinear Zernike filter

The key element of the nonlinear Zernike filter shown in Fig. 1c is an optically addressed phase spatial light modulator. For the nonlinear Zernike filter used in the experiments described here, a specially designed optically addressed liquid crystal light valve was manufactured. The schematic of the LCLV is shown in Fig. 7. The LCLV is based on parallel-aligned nematic LC with high refractive index anisotropy, and a transmissive, highly photo-sensitive, amorphous hydrogenated silicon carbide α -SiC:H film with diameter 12 mm and thickness near 1 μm . The photo-conductive film was fabricated by PeterLab Inc. (St. Petersburg, Russia). The nematic LC has low viscosity and an effective birefringence $\Delta n = 0.27$ for $\lambda = 0.514 \mu\text{m}$. The thickness of the LC layer is 5.2 μm .

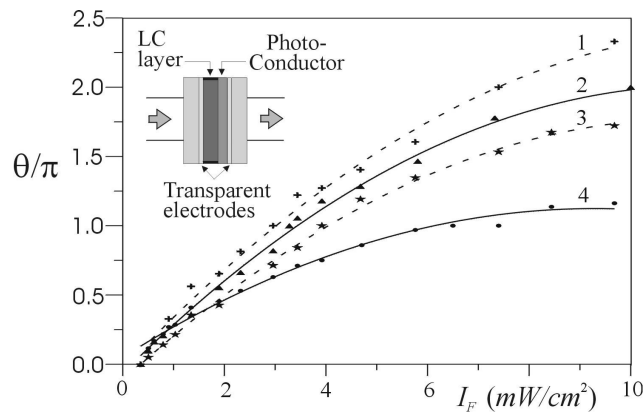


Fig. 7. Modulation characteristics of the LCLV: (1), (2) and (4) $\lambda = 0.514 \mu\text{m}$; and (3) $\lambda = 0.63 \mu\text{m}$. Applied voltage amplitudes are: (1) $V = 8.5$ Volts, (2) $V = 13$ Volts, (3) $V = 8.5$ Volts, and (4) $V = 16$ Volts. The schematic for the LCLV is shown at top left.

The intensity distribution on the LCLV photo-conductor film is transferred to an appropriate spatial distribution of the voltage applied to the LC layer. This results in a corresponding spatially distributed change of the LC molecule

orientation from planar to homeotropic.^{1,29} The LCLV is transmissive and operates in a pure phase-modulation mode when linearly polarized light with polarization axis parallel to the LC molecule director passes through the LC layer. The phase change $\theta = (2\pi/\lambda) d\Delta n$ introduced by the LCLV is determined by the LC layer thickness d and wavelength λ , and the effective LC birefringence Δn , dependent on such characteristics as the LC type, applied voltage, wavelength of the incident light, and temperature. Because the light-generated voltage pattern on the LC layer is dependent on the intensity distribution on the photo-conductor film, Δn is a function of both the intensity I_F on the LCLV photo-conductor layer and the amplitude of the sine wave voltage V applied to the LCLV electrodes.

Dependence of the phase shift θ on the light intensity and amplitude V of the applied voltage are shown in Fig. 7 (modulation characteristics). Near $\theta = \pi/2$, the phase modulation characteristics can be approximated by the linear function $\theta = \alpha I_F + c$, where c is a constant. The function $\alpha = \alpha(V, \lambda)$ characterizes the slope of the phase modulation characteristic, and can be controlled by changing the voltage applied to the LCLV. The characteristic time response of the LCLV was about 10 msec.

4.2. Nonlinear Zernike filter parameter optimization

We can estimate the requirements for the wavefront sensor input intensity level I_0 . For the lens of a given sensor with focal length L and wavelength λ we obtain $I_0 = (\lambda F / S)^2 I_F$.¹⁶ For fixed I_F and λ , the input intensity level I_0 can be decreased by choosing a lens with a short focal length. The focal length decrease is limited by the spatial resolution of the LCLV. Denote r_{res} as a characteristic spatial scale limited by the LCLV resolution. For the nonlinear Zernike filter, r_{res} should be smaller than the diffraction-limited focal spot size $a_F^{dif} \approx \lambda F/a$. This gives a rough estimate for both the minimal focal length $F_{min} \approx r_{res} a / \lambda$ and the minimum input intensity level $\min I_0 \approx [r_{res} / (\pi a)]^2 I_F$. For the LCLV used here, $r_{res} \approx 8 \mu\text{m}$. The spatial resolution was estimated from measurements of the LCLV diffractive efficiency. For a characteristic aperture radius of $a = 1 \text{ cm}$, $\lambda = 0.5 \mu\text{m}$, and LCLV optimal focal plane intensity level $I_F \approx 5 \text{ mW/cm}^2$, we obtain $F_{min} \approx 16 \text{ cm}$ and $\min I_0 \approx 0.3 \text{ nW/cm}^2$. Thus the nonlinear Zernike filter based on the optically controlled LC phase SLM can potentially perform high-resolution wavefront analysis under conditions of rather low input light intensity level.

4.3. Experimental results

The schematic of the experimental setup for the nonlinear Zernike wavefront sensor system is shown in Fig. 8. A laser beam from an Argon ($\lambda=0.514 \mu\text{m}$) or He-Ne ($\lambda=0.63 \mu\text{m}$) laser was expanded to a diameter of 20 mm and then passed through a multi-element LC HEX127 phase modulator from Meadowlark Optics, Inc. The LC modulator was used to introduce piston-type phase distortions $\varphi(r)$. This phase modulator has 127 hexagonal-shaped LC cells controlled by a personal computer (PC). Each cell is 1.15 mm in diameter with $36 \mu\text{m}$ spacing. To create phase distortions we also used an adaptive mirror (diameter 60 mm) from Xinetics, Inc. This mirror has 37 control electrodes and Gaussian-type influence functions, with a mechanical stroke of about $4 \mu\text{m}$. Dynamical phase aberrations were generated using an electrical heater with fan.

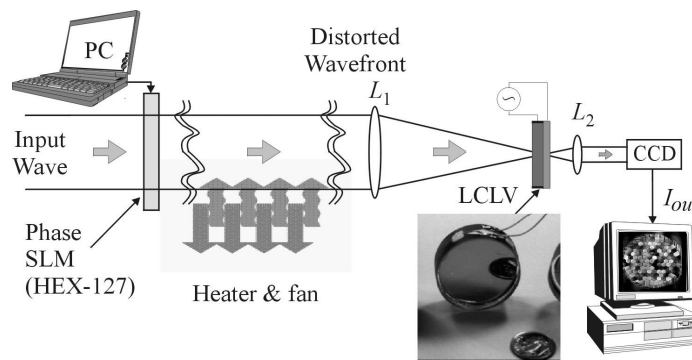


Fig. 8. Experimental setup of the LCLV based nonlinear Zernike filter with photo of the LCLV.

The focal length of the nonlinear Zernike filter front lens was $F_1 = 30$ cm. The second lens had a focal length of $F_2 = 10$ cm. The LCLV was placed in the common focal plane of lenses L_1 and L_2 . The CCD camera (Panasonic CCTV) with 771×492 pixels was placed in the rear focal plane of the lens L_2 . The registered intensity $I_{out}(\mathbf{r})$ was digitized and displayed on the PC monitor. The input wave intensity was near $I_0 \approx 3$ nW/cm².

Results of nonlinear Zernike wavefront sensor operation are shown in Fig. 9. In the experiments with the HEX127 phase modulator, the phase distortions were introduced into the input laser beam by applying random voltages $\{v_m\}$ to all 127 phase-modulator elements. The random values had a uniform probability distribution. The applied voltages caused random piston-type input wave phase shifts $\{\varphi_m\}$ leading to wavefront distortion. The typical sensor output intensity pattern shown Fig.9a corresponds to a wavefront distortion peak-to-valley amplitude of 2π . This output has good contrast and a high phase-intensity correlation coefficient value ($c_{\varphi,I} \approx 0.87$). The correlation coefficient was calculated using the measured phase modulation characteristic of the HEX127 (dependence of the phase shift φ_m on the applied voltage v_m).

Large amplitude aberrations ($\approx 4\mu\text{m}$) were introduced using the Xinçtics mirror with 100 volts applied to its central electrode. The resulting output intensity pattern is shown in Fig. 9b. The sensor's output image is quite different from the Gaussian-type function of the introduced phase aberration. The output pattern displays nonlinearity of the wavefront sensor occurring in the presence of large amplitude phase distortions. The nonlinear Zernike sensor was also used to visualize dynamical phase distortions created by a heater and fan. The dynamical pattern of the air flows was clearly seen despite the presence of large amplitude random tilts. A typical sensor output image is shown in Fig. 9c. The measured time response of the wavefront sensor was near 10 msec.

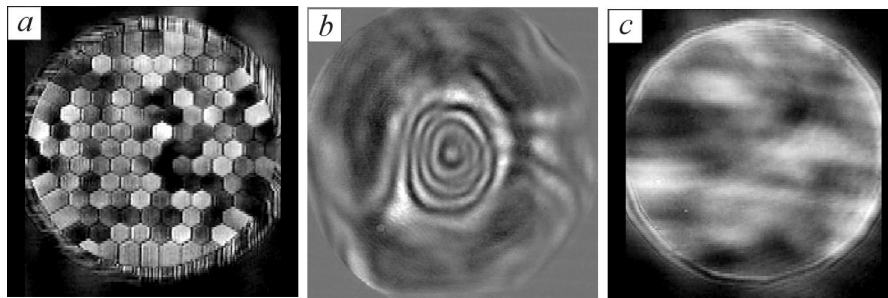


Fig. 9. Output patterns for the nonlinear Zernike filter with LCLV: left row $V=0$ Volts; right row $V=8.5$ Volts. Visualization of phase distortions generated by: (a) HEX127 LC phase SLM; (b) Xinçtics mirror; and (c) heater and fan. Picture (b) corresponds to $\lambda= 0.63\mu\text{m}$, and the others to $\lambda= 0.514\mu\text{m}$.

5. CONCLUSION

Advances in micro-electronics have made high-resolution intensity (imaging) sensors widely available. The situation is rather different for the sensing of spatial distributions for two other optical wave components: wavefront phase and polarization, for which sensors with spatial resolution and registration speed comparable to that of imaging sensors do not exist. For a number of applications the spatial distribution of the phase (phase image) is the only available and/or the only desirable information, and the demand for high-resolution, fast, inexpensive “phase imaging” cameras is continuously growing. Three requirements important for such “phase imaging” cameras are resolution, measurement accuracy, and speed. Until now we have had to choose between these requirements. High speed and measurement accuracy can be achieved using low-resolution wavefront sensors such as Shack-Hartmann and curvature sensors. On the other hand, high-resolution wavefront imaging sensors such as interferometers, phase contrast sensors, etc. are well known and widely used, but only for the registration and reconstruction of static or quasi-static phase images, as they do not provide sufficiently high operational speeds.

How is it possible to combine speed, accuracy and resolution in a single phase imaging camera? In this paper we have addressed this issue through an approach based on merging traditional phase contrast techniques with new wavefront sensor architectures that are based on micro-scale opto-electronic and computational technologies such as high-resolution

optically addressed phase SLMs, optical micro-mirror and LC arrays, and VLSI parallel analog computational electronics. This may potentially result in “phase imaging” cameras that provide high-resolution and high-speed wavefront sensing. The accuracy or linearity of the phase-intensity transformation performed by the wavefront sensor is the next challenge. Linearization of high-resolution wavefront sensor output can be achieved by incorporating high-resolution wavefront sensing and adaptive optics techniques.

ACKNOWLEDGEMENTS

We thank P.S. Krishnaprasad for helpful discussions, G. Carhart for assistance with the computer simulations, and J. C. Ricklin for technical and editorial comments. Work was performed at the Army Research Laboratory’s Intelligent Optics Lab in Adelphi, Maryland and was supported in part by grants from the Army Research Office under the ODDR&E MURI97 Program Grant No. DAAG55-97-1-0114 to the Center for Dynamics and Control of Smart Structures (through Harvard University), and the contract DAAL 01-98-M-0130 supported by the Air Force Research Laboratory, Kirtland AFB, NM.

REFERENCES

1. U. Efron, Ed., *Spatial Light Modulator Technology: Materials, Devices, and Applications*, Marcel Dekker Press, New York (1995).
2. M. C. Wu, “Micromachining for optical and opto-electronic systems”, *Proc. of the IEEE*, **85**, 1833 (1997).
3. G. V. Vdovin and P. M. Sarro, “Flexible mirror micromachined in silicon,” *Applied Optics*, **34**, 2968-2972 (1995).
4. S. Serati, G. Sharp, R. Serati, D. McKnight and J. Stookley, “128x128 analog liquid crystal spatial light modulator,” *SPIE*, **2490**, 55 (1995).
5. J.W. Hardy, J.E. Lefebvre and C. L. Koliopoulos, “Real-time atmospheric compensation,” *J. Opt. Soc. Am.*, **67**, 360-369 (1977).
6. D.G. Sandler, L. Cuellar, J.E. Lefebvre, et al, “Shearing interferometry for laser-guide-star atmospheric correction at large D/r_0 ,” *J. Opt. Soc. Am.*, **11**, 858-873 (1994).
7. J.W. Hardy, “Active Optics: a New Technology for the Control of Light,” *Proc. of the IEEE*, **66**, 651-697 (1978).
8. F. Roddier, “Curvature sensing and compensation: a new concept in adaptive optics,” *Appl. Opt.*, **27**, 1223-1225 (1988).
9. G. Rousset, “Wavefront sensors,” in *Adaptive Optics in Astronomy*, ed. F. Roddier, 91- 130, Cambridge University Press (1999).
10. R.W. Gerchberg and W. O. Saxon, “A practical algorithm for the determination of phase from image and diffraction plane pictures,” *Optik*, **35**, 237-246 (1972).
11. J.R. Fienup, “Phase retrieval algorithms: a comparison,” *Apl. Opt.*, **21**, 2758-2769 (1982).
12. V.Yu. Ivanov, V.P. Sivokon, and M.A. Vorontsov, “Phase retrieval from a set of intensity measurements: theory and experiment,” *J. Opt. Soc. Am.*, **9**(9), 1515-1524 (1992).
13. R.A. Gonsalves, “Phase retrieval from modulus data,” *J. Opt. Soc. Am.*, **66**, 961-964 (1976).
14. R.G. Paxman and J.R. Fienup, “Optical misalignment sensing and image reconstruction using phase diversity,” *J. Opt. Soc. Am.*, **5**, 914-923 (1988).
15. F. Zernike, “How I Discovered Phase Contrast,” *Science*, **121**, 345-349 (1955).
16. J.W. Goodman, “*Introduction to Fourier Optics*,” McGraw-Hill (1996).
17. S.A. Akhmanov and S. Yu. Nikitin, “*Physical Optics*,” Clarendon Press, Oxford (1997).
18. V.P. Sivokon and M.A. Vorontsov, “High-resolution adaptive phase distortion suppression based solely on intensity information,” *J. Opt. Soc. Am. A*, **15**(1), 234-247 (1998).
19. M.A. Vorontsov, “High-resolution adaptive phase distortion compensation using a diffractive-feedback system: experimental results,” *J. Opt. Soc. Am. A*, **16**(10), 2567-2573 (1999).
20. R. Dou, M.A. Vorontsov, V.P. Sivokon, and M.K. Giles, “Iterative technique for high-resolution phase distortion compensation in adaptive interferometers,” *Opt. Eng.*, **36**(12), 3327-3335 (1997).
21. R.N. Smartt, and W.H. Steel, “Theory and application of point-diffraction interferometers,” *Japanese Journal of Applied Physics*, 272-278 (1975).
22. *Selected Papers on Interferometry*. P. Hariharan, Editor, Optical Engineering Press (1991).
23. R. Angel, “Ground-based imaging of extrasolar planets using adaptive optics,” *Nature*, **368**, 203-207 (1994).
24. K. Underwood, J.C. Wyant and C.L. Koliopoulos, “Self-referencing wavefront sensor,” *Proc. SPIE*, **351**, 108-114 (1982).
25. A.D. Fisher and C. Warde, “Technique for real-time high-resolution adaptive phase compensation,” *Opt. Lett.* **87**, 353-355 (1983).
26. M.A. Vorontsov, A.F. Naumov and V.P. Katulin, “Wavefront control by an optical-feedback interferometer,” *Opt. Comm.* **71**(1-2), 35 (1989).
27. *Learning on Silicon*, eds. G. Cauwenberghs and Magdy A. Bayoumi, Kluwer Academic, Boston, Dordrecht, London (1999).
28. A.G. Andreou, and K.A. Boahen, *Analog Integrated Circuits and Signal Processing*, **9**, 141 (1996).
29. V.G. Chigrinov, *Liquid Crystal Devices: Physics and Applications*, Artech House, Boston (1999).
30. J.W. Goodman, *Statistical Optics*, Wiley, New York (1985).
31. L.C. Andrews, “An analytic model for the refractive index power spectrum and its application to optical scintillations in the atmosphere,” *J. Mod. Opt.* **39**, 1849-1853 (1992).
32. D.L. Fried, “Statistics of a Geometric Representation of Wavefront Distortion,” *J. Opt. Soc. Am.*, **55**, 1427-1435 (1965).